Journal of Colloid and Interface Science 704 (2026) 139381

Contents lists available at ScienceDirect

Journal of Colloid And Interface Science

journal homepage: www.elsevier.com/locate/jcis

Regular Article

Numerical investigation of realistic core-shell microgels: Insights on two- and three-body effective interactions

Gerardo Campos-Villalobos [a,*], Rodrigo Rivas-Barbosa [b], Emanuela Zaccarelli [a,*]

[a] CNR-ISC and Department of Physics, Sapienza University of Rome, p.le A. Moro 2, 00185 Rome, Italy
[b] School of Physics and Astronomy, University of Edinburgh, Edinburgh, EH9 3FD, United Kingdom

GRAPHICAL ABSTRACT

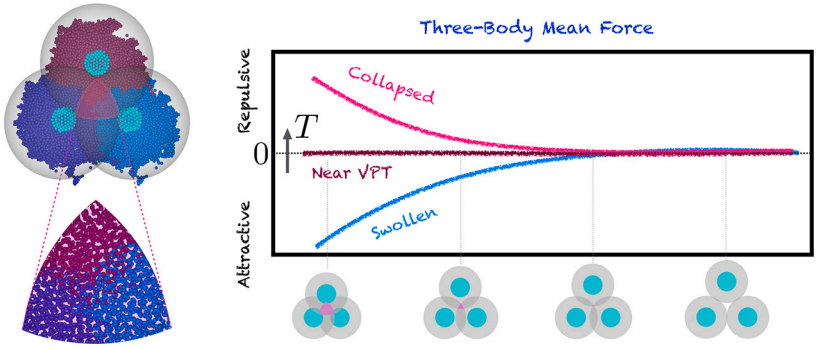

ARTICLE INFO

Keywords:
Core-shell microgels
Molecular simulation
Coarse-grained models
Effective interactions
Many-body effects

ABSTRACT

Core-shell (CS) microgels–comprising a solid core chemically linked to a crosslinked polymer shell–are an important class of stimuli-responsive colloids widely employed for both fundamental and applied studies. Despite extensive experimental investigations, their numerical modeling remains underdeveloped; in particular, a detailed, temperature-resolved insight of their effective interactions is missing. While pairwise descriptions known for standard microgels are expected to be partially extensible to CS-microgels, the effect of the solid core and in turn, the extent and character of many-body contributions remain elusive. To clarify these open issues, this work introduces a computational method to generate realistic CS-microgels at different crosslinker concentrations, accurately reproducing the structure of experimental silica core–poly-*N*-isopropylacrylamide (pNIPAM) shell microgels at different temperatures across the Volume Phase Transition (VPT) and for different shell-to-core ratios. After validating the model, effective interactions between CS-microgels are calculated, extracting not only two-body interactions but also providing the first quantitative investigation of three-body effects in any microgel system. The present findings show that, albeit small, the latter contributions are non-negligible and exhibit an intriguing sign reversal: while being predominantly attractive at low temperatures, they become repulsive at high ones, nearly canceling out at the VPT. These results reveal a subtle interplay between microgel architecture, temperature and many-body correlations, with direct implications on the design of responsive soft materials and their mutual interactions.

* Corresponding authors.
E-mail addresses: gerardodejesuscamposvillalobos@cnr.it (G. Campos-Villalobos), emanuela.zaccarelli@cnr.it (E. Zaccarelli).

https://doi.org/10.1016/j.jcis.2025.139381
Received 13 August 2025; Received in revised form 27 October 2025; Accepted 30 October 2025

Available online 5 November 2025

1. Introduction

Core-shell (CS) microgels are a versatile class of colloidal particles that combine the rigidity of a solid core with the softness of a crosslinked polymer shell [1]. From a technological point of view, the relative ease with which the characteristics of CS microgels can be controlled during synthesis results in a wide range of applications across disciplines [2,3]. Examples of the design possibilities available when working with these particles include the freedom to choose the core-to-shell ratio, the crosslinking content [4], as well as the shape of the core, which can even be anisotropic [5]. In terms of composition, the choice of poly-N-isopropylacrylamide (pNIPAM) for the shell is a rather obvious one, providing thermal responsivity to the CS-microgels. In particular, the network undergoes a transition from a swollen to a collapsed state when increasing the temperature, with the effect being the most predominant around the so-called volume phase transition temperature VPTT $\sim 32\,^{\circ}$C [6]. Equally important is the selection of the core material, for instance, silica is preferred for the assembly of photonic crystals [7], while gold is used for nanoplasmonics [8]. Hybrid microgel particles incorporating active (e.g., optically or magnetically) nanoparticles such as gold or silver, have also found applications in the field of sensing [9,10] and catalysis [11]. Because "core-shell microgel" is used ambiguously in the literature–sometimes also for microgels with a densified polymer network at their center–we note this broader usage here but, for clarity, we use core-shell microgel exclusively to denote particles with rigid/non-polymeric cores and do not consider densified-soft-core microgels.

In addition to their potential applications, CS-microgels serve as important model systems for fundamental research due to their complex structural and rheological behaviors [12]. In particular, investigations have focused on the arrangement of these microgels at liquid-liquid interfaces [13,5], where the relative affinity of the core and shell to the two liquid phases can be tuned [14]. Furthermore, recent work has explored the fluid-crystal transition of silica-core, pNIPAM-shell microgels using small-angle scattering experiments, distinguishing their behavior from that of standard hard-sphere colloids [15]. Notably, unlike conventional microgels, CS-microgels enable a direct determination of the actual volume occupied by these deformable soft particles. This property makes them ideal model colloids for experimentally identifying phase transition boundaries, which are driven by temperature variations and reflect the well-known tunable nature of effective interactions in microgels [16].

Despite the huge amount of experimental works, numerical simulations of CS-microgels are still scarce due to the lack of an established coarse-grained model at the monomer scale, that would allow for an accurate and efficient modeling at the single particle level. Few earlier efforts were based on the use of an ordered underlying topology of the polymeric shell [13,17], which is quite different from the disordered nature of the shell synthesized in experiments.

To fill this gap, in this work we build on our well-established *in silico* microgel model [18], previously shown to quantitatively describe the experimental form factors of pNIPAM microgels across the VPT [19], and extend it to the case of core-shell ones. We thus broaden our numerical protocol to prepare CS-microgels with realistic internal structures at different crosslinker concentrations and core-to-shell ratios, and compare the simulation results with available experimental data from the literature. In all cases, we find an overall excellent agreement with experiments, thus providing a reliable model for CS microgels *in silico*.

The validated model provides an invaluable platform for investigating the effective interactions between CS microgels. The presence of a well-defined, non-deformable core is particularly convenient, as it permits integrating out the degrees of freedom of the polymeric network and deriving a core-only, coarse-grained description in the spirit of the effective one-component Hamiltonian for colloidal systems [20,21]. In particular, the rigid core furnishes natural reaction coordinates (the core centers), which makes constrained sampling and force-based extraction of two- and three-body contributions numerically simpler than in microgels with architectures lacking a rigid reference component. These interactions are not only essential for constructing coarse-grained (single-site) models that retain the key features of the underlying microgel architecture while enabling simulations of many-body systems at larger scales or higher concentrations, but their understanding is also crucial to rationalize experimental behavior. By means of constrained Molecular Dynamics simulations, we thus first extract the effective two-body interactions of CS microgels, confirming their temperature dependence and revealing an approximate Hertzian-like repulsive behavior below the VPT, which, as expected turns into an attractive interaction at higher temperatures. In addition, for the first time, we study the triplet interactions of such deformable colloids, identifying a subtle temperature dependence: the three-body contribution, which becomes relevant at close interparticle distances, exhibits a sign reversal—being predominantly attractive in the swollen state and repulsive in the collapsed one, passing through an apparent zero-crossing. We finally propose plausible explanations for this intriguing behavior.

2. Methods

2.1. In Silico synthesis of core-shell microgels

In order to construct the CS-microgels, we slightly adjust the method introduced in Ref. [18] for standard microgels to take into account the presence of a spherical rigid core of radius R_c. The latter is built adopting a rigid-composite-bead representation, in which small particles are distributed on the surface of the "large" core and treated collectively as a rigid body. Then, we rely on the self-assembly of patchy particles onto the core. To this aim, a binary mixture of patchy particles of mass m and diameter σ — the unit of length — is employed to assemble the disordered polymeric network in a spherical volume of radius $Z > R_c$. Patchy particles have four and two patches each, representing crosslinkers and monomers, respectively. In addition, the core beads are also decorated with a single patch, onto which monomers or crosslinkers can bind. All patchy interactions are identical and details of the employed potential can be found in previous works [18,19]. A swap bonding mechanism [22] is also used to speed up the self-assembly process.

The total number of particles N is chosen to set a reduced number density $\rho\sigma^3 = N\sigma^3/[4\pi/3(Z^3 - R_c^3)] \approx 0.08$ in the shell, which has been established previously by comparison to experiments for standard and hollow microgels [19,23]. The molar concentration of the crosslinkers c varies between 1 and 15%, which is the range typically explored in experimental systems [24,15]. To reproduce the well-known inhomogeneous distribution of crosslinkers within the microgel, due to their faster reactivity with respect to NIPAM monomers, we also apply a phenomenological force on the crosslinkers [19].

Brownian Dynamics simulations of the assembly are performed using the oxDNA simulation package [25] at fixed low temperature $T = 0.01\epsilon/k_B$, where k_B is the Boltzmann constant and ϵ sets the scale of interparticle interactions. While the core-forming particles are kept fixed, the overdamped Langevin equations of motion of the remaining particles are integrated with a timestep $\delta t = 0.002\tau$, where $\tau = \sqrt{m\sigma^2/\epsilon}$ is the time unit and m the mass of the patchy particles. The simulations are left running until almost all particles ($96 - 99.8\%$, depending on system parameters) are connected into the largest cluster. At this point, the simulation is stopped and only such largest cluster is retained, comprising the particles from the shell network and the solid core. Interestingly, we find that a full core coverage is never achieved. Instead, only a fraction of the core particles form bonds with the shell particles. This fraction ranges from 20 to 70%, depending on the simulation parameters.

2.2. Core-shell microgel simulations

Following the assembly, the obtained CS-microgel is fixed with the resulting topology by substituting patchy interactions with the stan-

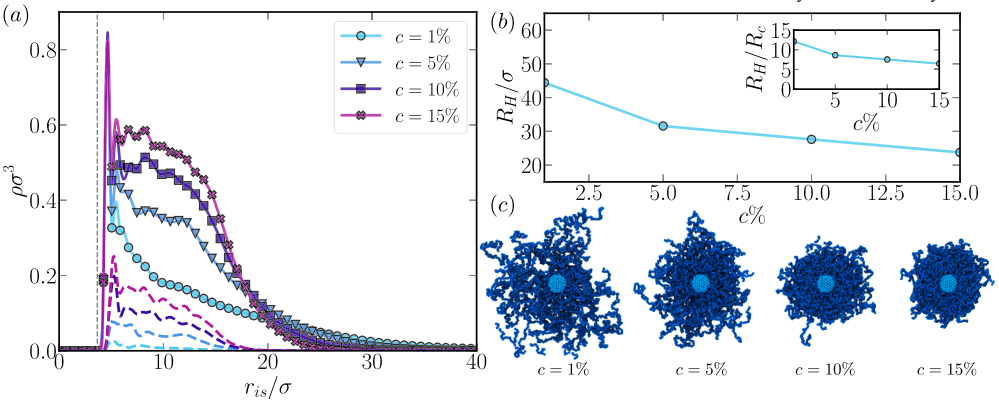

Fig. 1. Structure of CS-microgels in the swollen state. (a) Average density profiles of CS-microgels with varying crosslinker concentrations c at $\alpha = 0$, showing the overall (symbols) and crosslinker (dashed lines) distributions as a function of radial distance r_{is} from the center of mass of the solid core. The vertical grey dashed line marks the core radius R_c; (b) hydrodynamic radius R_H, as a function of c and corresponding R_H/R_c ratio reported in the inset; (c) Representative snapshots of CS-microgels, where the polymeric shell (interconnected blue beads) is sliced to reveal the rigid solid core (cyan spheres).

dard bead-spring potential for polymeric systems [26] as in previous works [18,19]. This amounts to excluded volume interactions, modeled by the Weeks-Chandler-Andersen (WCA) potential, among all beads,

$$\phi_{\mathrm{WCA}}(r_{ij}) = \begin{cases} 4\epsilon\left[\left(\frac{\sigma}{r_{ij}}\right)^{12} - \left(\frac{\sigma}{r_{ij}}\right)^{6}\right] + \epsilon & \text{if } r_{ij} \le 2^{1/6}\sigma \\ 0 & \text{otherwise}, \end{cases} \tag{1}$$

where ϵ sets the energy scale and $r_{ij} = |\boldsymbol{r}_i - \boldsymbol{r}_j|$ is the distance between i and j beads, plus a Finite-Extensible-Nonlinear-Elastic (FENE) contribution for bonded beads, which reads as,

$$\phi_{\mathrm{FENE}}(r_{ij}) = -k_F R_0^2 \ln\left[1 - \left(\frac{r_{ij}}{R_0}\right)\right] \quad \text{if } r_{ij} < R_0 \tag{2}$$

where $k_F = 15\epsilon/\sigma^2$ is the bond constant and $R_0 = 1.5\sigma$ is the maximum allowed bond distance. In order to implicitly take into account the change of affinity between the solvent and NIPAM upon increasing temperature, we use the solvophobic potential $\phi_\alpha(r_{ij})$ [27,28]. This can be written as,

$$\phi_\alpha(r_{ij}) = \begin{cases} -\epsilon\alpha & \text{if } r_{ij} \le 2^{1/6}\sigma \\ \frac{1}{2}\epsilon\alpha\left[\cos\left(\zeta\left(\frac{r_{ij}}{\sigma}\right)^2 + \chi\right) - 1\right] & \text{if } 2^{1/6}\sigma < r_{ij} \le R_0 \\ 0 & \text{otherwise}, \end{cases} \tag{3}$$

where $\zeta = \left[\pi(2.25 - 2^{1/3})\right]^{-1}$, $\chi = 2\pi - 2.25\zeta$, and α controls the strength of the attractive interaction. The solvophobic parameter α can thus be interpreted as an effective temperature, and as established in previous studies on several types of microgels [19,23], good solvent conditions are attained at $\alpha = 0$, while the collapsed state is reached for $\alpha \sim 0.8 - 1.0$, with the VPT occurring around $\alpha \sim 0.6$ [29]. It should be noted that even though the cores of the assembled CS-microgels generally do not reach "full coverage", i.e., that only a fraction of the discrete surface sites on the rigid core forms covalent bonds with the shell network, these bonds anchor the shell to the core permanently, effectively preventing any sliding of the shell over the core or monomer penetration into the core.

Molecular Dynamics (MD) simulations of CS-microgels are performed in the canonical ensemble using the LAMMPS simulation package [30]. The core-forming beads are kept frozen and only the equations of motion of the beads comprising the polymeric network are integrated with a timestep $\delta t = 0.002\tau$, using a Nosé-Hoover thermostat to maintain the temperature at $T = 1.0\epsilon/k_B$. Unless stated otherwise, the simulations are conducted for 2×10^7 steps, with statistics on observables accumulated over the final 1.5×10^7 steps. For the quantities reported throughout, we compute standard errors (SE) from a five-block analysis of each trajectory ($\mathrm{SE} = \mathrm{SD}/\sqrt{5}$), where SD is the sample standard deviation of the block means. Since the resulting error bars are typically smaller than the symbol size, we do not display them for clarity.

3. Results

3.1. Characterization of core-shell microgels

We begin by analyzing the structure and swelling behavior of CS-microgels with a fixed core radius, $R_c = 3.66\sigma$, assembled under a confining spherical region with $Z = 33\sigma$, at different crosslinker concentrations $c = 1, 5, 10, 15\%$. Depending on c, the resulting number of crosslinked monomers composing the polymeric shell varies around $N \sim 1.1 \times 10^4 - 1.2 \times 10^4$. The core dimensions and the shell thickness, ΔR, are chosen to mimic the experimental silica-PNIPAM CS-microgels with $c = 15\%$ recently used by Hildebrandt et al. [15] to study the temperature induced fluid-solid transition in dense packings.

The internal distribution of monomers within the different CS-microgels in the swollen state, i.e., for $\alpha = 0$, can be appreciated in Fig. 1(a), where we report the density profiles

$$\rho_\iota(r_{is}) = \frac{1}{\Omega(r_{is})}\left\langle \sum_{i=1}^{N_\iota} \delta(|\boldsymbol{r}_i - \bar{\boldsymbol{r}}_c| - r_{is}) \right\rangle, \tag{4}$$

where ι denotes the bead species, either crosslinker (CL) or all bead types (P), $\boldsymbol{r}_i$ is the position of bead i, and $\bar{\boldsymbol{r}}_c$ is the position of the center of mass of the solid core. The quantity $\Omega(r_{is})$ is the volume of a spherical shell of thickness Δr_{is} at radial position r_{is}, i.e., $\Delta r_{is} = 4\pi r_{is}^2 \Delta r_{is}$. Angle brackets $\langle\cdot\rangle$ indicate a time average. By inspecting the crosslinker profiles $\rho_{CL}(r_{is})$ (dashed lines in Fig. 1(a)), we can see that they are primarily located toward the inner section of the CS-microgel shell. An interesting feature is that, in the close vicinity of the solid core around $r_{is} \sim R_c$, the polymeric network forms some layers, that eventually disappear at a large distance. This layering near the solid core aligns with previous experimental findings, which show that to properly fit the measured form factors of silica-PNIPAM CS-microgels in the swollen state, the model must include a dense layer near the silica core [24]. It is clear that although the confinement Z is identical during the assembly of the CS-microgels, the overall dimensions of the resulting particles are sensitive to the value of c. More specifically, as the amount of crosslinker increases, the $\rho_P(r_{is})$-profiles decay to zero over shorter distances, indicating more compact shell structures. The characteristic way in which such profiles decay at large r_{is}, in particular, the "tails", is the result of the fluctuations of the corona, including the loose dangling chains in its outer part, which can be appreciated in representative simulation snapshots shown in Fig. 1(c).

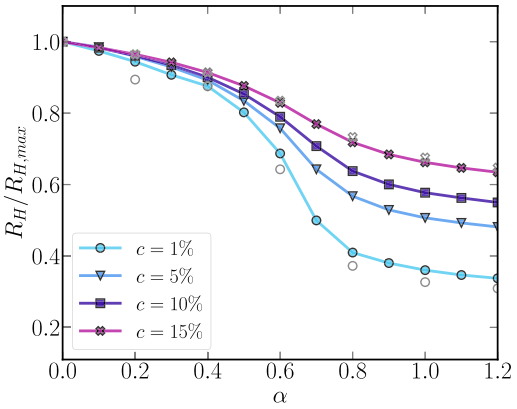

Fig. 2. Swelling curves of CS-microgels. Normalized hydrodynamic radius $R_H/R_{H,max}$ as a function of the solvophobic parameter α for CS-microgels of different crosslinker concentration, c. Open gray symbols correspond to values for standard microgels assembled without a solid core with $c = 1$ (circles) and 15% (stars).

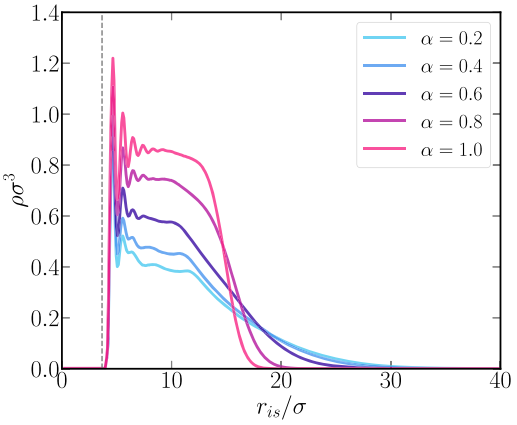

Fig. 3. Density profile of CS-microgels across the swelling curve. Average density profiles of CS-microgels with crosslinker concentration $c = 5\%$ for different values of α across the swelling curve, showing the distribution of all monomers as a function of radial distance r_{is} from the center of mass of the solid core. The vertical gray dashed line marks the core radius R_c.

To determine the effective size of the CS-microgels, we compute their hydrodynamic radii as [31,32]

$$R_H = \left\langle 2\left[\int_0^\infty \frac{1}{\sqrt{(a_1^2+\theta)(a_2^2+\theta)(a_3^2+\theta)}}\, d\theta\right]^{-1}\right\rangle, \tag{5}$$

where $a_i = \sqrt{3\lambda_i}$ for $i = 1,2,3$, and the λ_i are the eigenvalues of the gyration tensor built on the convex-hull vertices of the CS-microgel. This procedure was previously shown to yield results in good qualitative agreement with experiments for standard microgels [32]. Because the rigid spherical core lies strictly inside this hull, it does not contribute hull vertices and therefore does not enter the semi-axes a_i explicitly. Any influence of the core on R_H is indirect, via its mechanical constraint on the shell that shapes the outer hydrodynamic envelope.

The hydrodynamic radius, as well as the ratio R_H/R_c, for each CS-microgel are reported in Fig. 1(b). As expected, R_H increases as c decreases for swollen CS-microgels assembled under identical confinement Z and density ρ conditions.

Turning to examine the temperature behavior of the CS-microgels, we calculate the swelling curves as the ratio between the overall hydrodynamic radius for a given value of the solvophobic parameter α, $R_H(\alpha)$, over its value in the swollen state at $\alpha = 0$, where it takes the largest value $R_H(\alpha = 0) = R_{H,max}$. The results are shown in Fig. 2, where we also include for reference the swelling curves of standard microgels assembled in the absence of a solid core at the same Z and ρ, for $c = 1$ and 15%. It is evident that the behavior exhibited by the CS-microgels largely aligns with that of standard microgels, with a VPT that is virtually independent of c, occurring at an effective temperature $\alpha \approx 0.63$, and a collapsed state reached at $\alpha \approx 0.8$. Since the solid core is effectively "insensitive" to changes in temperature, CS-microgels can be intuitively expected to show a less pronounced reduction in R_H with α compared to their coreless counterparts, especially when the ratio R_H/R_c becomes small. Nevertheless, for the present system, such differences are barely noticeable, probably due to the relatively large R_H/R_c ratio.

In Fig. 3, we show how the density profile of the CS-microgel with $c = 5\%$ evolves with the solvophobic parameter α along the swelling curve, ranging from $\alpha = 0.2$ to $\alpha = 1.0$. We first note that below the VPT, i.e., for $\alpha \leq 0.6$, the density profiles resemble those at $\alpha = 0$: they exhibit layering near the solid core, followed by a compact region and a gradual decay around $r_{is} \sim 10{-}12\,\sigma$. Above the VPT, the compact region extends over a larger distance and it is followed by a sharper decay, while the layering near the core remains pronounced. The observation of persistent layering contrasts with experimental findings in Ref. [24], where CS-microgels with a similar c appeared to undergo a transformation in the collapsed state—losing the dense core-adjacent layer and instead displaying a nearly uniform ("box-like") density profile. However, the CS-microgels studied in Ref. [24] possessed a relatively smaller shell-to-core ratio. In the following section, we demonstrate that such a transformation can indeed occur in CS-microgels with comparable geometric characteristics.

3.2. Validation of the assembly method: comparison to experiments

To validate our assembly method, we consider three silica core-shell microgels studied experimentally in the literature, that differ among themselves in both architecture and composition. We refer to these microgels as CS_1, CS_2, and CS_3 and their parameters are as follows: CS_1: $R_H(\alpha = 0)/R_c \approx 7.6$, $c = 15\%$; CS_2: $R_H(\alpha = 0)/R_c \approx 3.6$, $c = 5.4\%$; and CS_3: $R_H(\alpha = 0)/R_c \approx 2.5$, $c = 5.4\%$. CS_1 corresponds to the CS-microgel with $c = 15\%$ described in the previous Subsection, designed to model the experimental system recently studied by Hildebrandt et al. [15]. The parameters for CS_2 and CS_3 are instead designed to mimic experimental CS-microgels reported by Dubbert et al. [24]. We note that for these latter ones, to ensure a large enough shell, the assembly is performed around a core with a larger radius ($R_c = 14.46\sigma$) than that of CS_1, as visible from the representative snapshots of the three CS-microgels in the swollen state displayed in Fig. 4(b).

To compare the calculated swelling curves of the three CS-microgels with experimental results, obtained via temperature-dependent dynamic light scattering measurements [15,24], we use a linear mapping between the solvophobic parameter α and the absolute temperature, as done in previous works [19,33].[1] Once α is mapped to T, we simply scale our simulation length units, σ, to the experimental ones (here in nm). The swelling curves of the three model CS-microgels are compared with the corresponding experimental ones in Fig. 4(a), which show the transition from the swollen state (S) at low temperatures to the collapsed state (C) for high temperatures. The VPT temperatures are $T_{\mathrm{VPT}} \approx 308$ K for CS_1 and $T_{\mathrm{VPT}} \approx 305$ K for CS_2 and CS_3. In our model units, the transition still occurs around $\alpha \sim 0.6$ and the collapsed state is reached at $\alpha \sim 0.8$. Clearly, since the amount of crosslinker is larger in CS_1 than

[1] To determine the coefficients A and B of the linear mapping, $T = A + B\alpha$ (in K), we match the swollen state at $\alpha = 0$ (temperature T_0) and at $\alpha = \alpha_{\mathrm{VPT}} = 0.63$ (temperature T^*), yielding $A = T_0$ and $B = (T^* - T_0)/\alpha_{\mathrm{VPT}}$. The resulting parameters are: CS_1: $A = 290.33$ K, $B = 28.28$ K; CS_2 and CS_3: $A = 289.16$ K, $B = 25.38$ K. These findings are fully compatible with the (α, T) mapping already established for standard microgels [19,33].

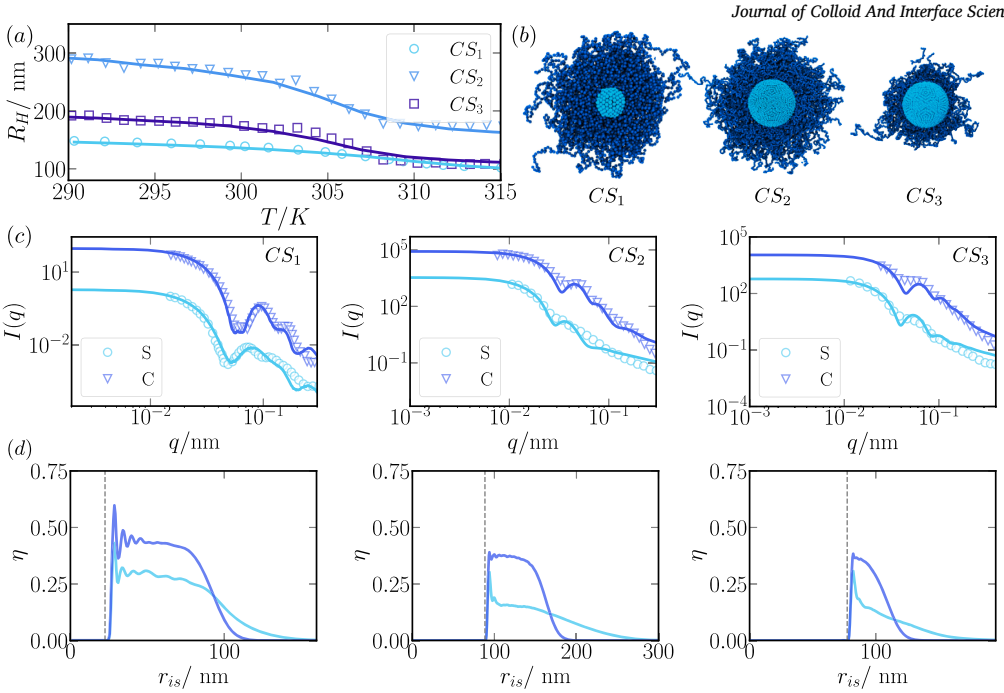

Fig. 4. Comparison to experimental data. (a) Hydrodynamic radius, R_H, of CS-microgels CS_1, CS_2, and CS_3 as a function of temperature, T. Open symbols correspond to experimental data, taken from Ref. [15] for CS_1 and from Ref. [24] for CS_2 and CS_3 microgels; whereas lines are the results of simulations. The transformation from simulation units to real (experimental) units is described in the text. (b) Slice view of typical equilibrium configurations for the three CS-microgels under consideration. (c) Form factors, $I(q)$, of CS-microgels in their low-temperature swollen (S) and high-temperature collapsed (C) states. Open symbols represent experimental SANS/SAXS data from Refs. [15,24], while lines correspond to (scaled) simulation data computed using Equation (6). (d) Radial polymer volume fraction profiles, $\eta(r_{is})$, of the three CS-microgels in the S and C states obtained from MD simulations. The vertical gray dashed lines mark the core radius.

in CS_2 and CS_3, the de-swelling is slightly more pronounced in the latter ones. This trend is well captured by our numerical CS-microgel model, which yields an overall good agreement with experimental data.

Experimentally, microgel density profiles are typically not directly measurable but can be inferred from the form factors, measured via neutron or X-ray scattering as a function of the wavenumber q. To demonstrate the robustness of our method, we compute the form factors of CS-microgels and compare them with experimental SANS/SAXS data. To accurately capture the core-shell architecture in our calculations, we regard each microgel as a binary system composed of $N_m = N$ monomers and a single core particle ($N_c = 1$), with respective diameters σ and $d_c = 2R_c$. In this way, the scattering intensity $I(q)$, defined as the time-averaged squared magnitude of the scattered field as a function of the momentum transfer, q, in reciprocal space reads:

$$
\begin{aligned}
I(q) = \Bigg\langle & b_m^2(q)\left[\left(\sum_{j=1}^{N_m}\cos(\boldsymbol{q}\cdot\boldsymbol{r}_j)\right)^2 + \left(\sum_{j=1}^{N_m}\sin(\boldsymbol{q}\cdot\boldsymbol{r}_j)\right)^2\right] \\
& + b_c^2(q)\left[\left(\sum_{k=1}^{N_c}\cos(\boldsymbol{q}\cdot\boldsymbol{r}_k)\right)^2 + \left(\sum_{k=1}^{N_c}\sin(\boldsymbol{q}\cdot\boldsymbol{r}_k)\right)^2\right] \\
& + 2b_c(q)b_m(q)\sum_{j=1}^{N_m}\cos(\boldsymbol{q}\cdot\boldsymbol{r}_j)\sum_{k=1}^{N_c}\cos(\boldsymbol{q}\cdot\boldsymbol{r}_k) \\
& + 2b_c(q)b_m(q)\sum_{j=1}^{N_m}\sin(\boldsymbol{q}\cdot\boldsymbol{r}_j)\sum_{k=1}^{N_c}\sin(\boldsymbol{q}\cdot\boldsymbol{r}_k)\Bigg\rangle,
\end{aligned}
\tag{6}
$$

where $\boldsymbol{q}$ is the scattering vector, $b_m(q)$ and $b_c(q)$ denote the single-particle scattering amplitudes of the monomer and solid core, respectively; each equals the scattering-length density (SLD) contrast multiplied by the particle volume and sphere form factor. Assuming that the monomers and the solid core are perfectly spherical, the amplitude for species ι with corresponding radius R_ι, is calculated as

$$
b_\iota(q) = R_\iota^3 \Delta_n \frac{3}{(qR_\iota)^3}[\sin(qR_\iota) - qR_\iota\cos(qR_\iota)], \tag{7}
$$

where $\Delta_n = n_p - n_0$ is the SLD contrast and n_p and n_0 correspond to "material properties" of the particle and the suspension medium, respectively. In the case of light scattering, these represent refractive indices, while for scattering of X-rays or neutrons, they correspond to electron or nuclear scattering length densities [34]. Furthermore, in order to account for the experimental resolution of the measurements, $\Delta q/q$, which essentially dampens the peaks in the $I(q)$ curves, we apply a Gaussian smoothing (correction) to our numerical data. More specifically, for each point, q_i, we compute a Gaussian-weighted average over $\mathcal{N}_s$ shifted versions of the function $I(q)$ as: $I(q_i) = \sum_{j=1}^{\mathcal{N}_s}\omega(dq_j)I(q_i + dq_j)$, where $\omega(dq_j)$ are Gaussian weights, and dq_j are the shifted points. In practice, in order to match the experimental $I(q)$ at low temperatures (S state), we optimize the ratio of the SLD contrasts to the medium and set the resolution to a typical experimental value of $\Delta q/q \sim 10\%$. After scaling the numerical data to match the $I(q)$'s in the S-state, we use the same constants to scale the curves computed for the C-state at high temperature. In the case of CS_1, the experimental temperatures for the S and C states are $T_S = 293.15$ K and $T_C = 313.15$ K [15], respectively, while for CS_2 and CS_3, such temperatures are $T_S = 293.15$ K and $T_C = 323.15$ K.

In Fig. 4(c), we report a comparison between the form factors of the three simulated CS-microgels and the corresponding experimental data reported in Refs. [15,24]. The Figure includes profiles for both the S and C states. We note that the smoother appearance of the experimental CS_2 and CS_3 curves may reflect a combination of polydispersity in core size and shell thickness; differences between the CS_1 (SAXS) and CS_2/CS_3 (SANS) measurements could also play a role. In all cases, the simulated and experimental results show good qualitative agreement, particularly in the low- and intermediate-q regions. Minor discrepancies become noticeable at high q (small length scales), arising from limitations in spatial resolution inherent to the coarse-grained nature of the numerical model. As discussed in the previous section, fits to the experimentally measured SANS-$I(q)$ profiles of CS-microgels in Ref. [24]

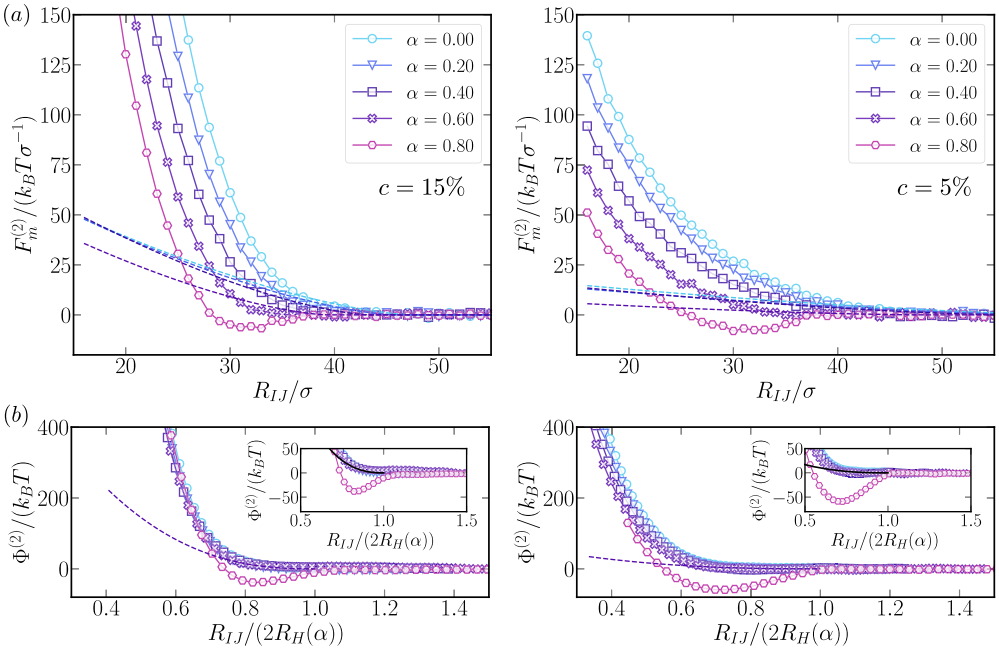

Fig. 5. Effective two-body interactions of CS-microgels. (a) Two-body mean forces $F_m^{(2)}$ as a function of the separation distance for different α values across the swelling curve. Symbols correspond to values obtained from constraint-bias MD simulations, whereas dotted lines for $\alpha \leq 0.60$ are Hertzian force fits. (b) The corresponding effective two-body potentials $\Phi^{(2)}$ as a function of the separation distance, R_{IJ}, scaled by the approximate temperature-dependent CS-microgel diameter $2R_H(\alpha)$. In the insets, the potentials are magnified to better visualize the minima of the curves for $\alpha = 0.8$. The dashed lines (and the solid black lines in the insets) correspond to Hertzian potential fits for $\alpha = 0.60$.

suggest that, in the case of relatively thin polymer shells and low c, the density profiles lose the layering near the solid core when transitioning from the swollen to the collapsed state. Specifically, the system reported in Ref. [24] corresponds to the CS_3 microgel considered in the present work. In Fig. 4(d), this scenario is indeed verified, as the volume fraction profiles, defined as $\eta(r_{is}) \equiv \pi\rho(r_{is})\sigma^3/6$, clearly show that the "big" layer in the vicinity of the solid core characterizing the S-state, is essentially absent in the C-state. Interestingly, we find that in the case of CS_2, a very similar behavior arises, while in the sample CS_1, the strong oscillations persist across the swelling curve, pointing to a non-trivial dependence of the monomer organization on the geometric parameters. We attribute the persistence of oscillations in CS_1 to its thicker, more highly crosslinked corona, which helps maintaining a sharper core-corona interface and preserves short-wavelength density correlations across the VPT. Altogether, these observations validate the ability of our assembly method to generate "realistic" CS-microgels.

3.3. Effective core-shell microgel interactions

Having validated our assembly method, we now proceed to analyze the effective interactions of CS-microgels. We focus on a single CS-microgel architecture, namely CS_1, at two crosslinker concentrations $c = 5\%$ and 15%.

3.3.1. Two-body interactions

We start by determining the effective pair forces of two CS-microgels as a function of the separation distance between the centers of their solid cores, $R_{IJ} = |\boldsymbol{R}_{IJ}| = |\boldsymbol{R}_I - \boldsymbol{R}_J|$, using constrained-bias MD simulations where the mean force profile, corresponding to the (negative) gradient of the effective two-body potential, $\boldsymbol{F}_m^{(2)}(R_{IJ}) = -\nabla_{\boldsymbol{R}_{IJ}}\Phi^{(2)}(R_{IJ})$, is measured [35]. To sample the mean force in a MD simulation, the centers of mass of the CS-microgels' cores, $\boldsymbol{R}_I$ and $\boldsymbol{R}_J$, are kept fixed, and the (scalar) mean force is calculated as the average force in the direction of their connecting line as:

$$F_m^{(2)}(R_{IJ}) = \frac{1}{2}\left\langle (\boldsymbol{F}_J - \boldsymbol{F}_I)\cdot \boldsymbol{R}_{IJ}/R_{IJ}\right\rangle_{NVT,\boldsymbol{R}_I,\boldsymbol{R}_J}, \tag{8}$$

where $\boldsymbol{F}_I$ and $\boldsymbol{F}_J$ are the total instantaneous (vectorial) forces acting on the cores of CS-microgels I and J, respectively. The effective two-body potential is directly obtained by integration of the mean force along R_{IJ}

$$\Phi^{(2)}(R_{IJ}) = \int_{R_{IJ}}^{\infty} F_m^{(2)}(R'_{IJ})\,dR'_{IJ}. \tag{9}$$

The effective two-body forces and their associated potentials of mean force for CS-microgels with $c = 5\%$ and 15% are shown in Fig. 5(a) and (b), respectively, for different α values. In the latter plots, to give an immediate sense of the spacing between microgels, the distance is scaled by the value of the approximate particle diameter at the corresponding effective temperature, i.e., $2R_H(\alpha)$, above which the potential goes to zero. As expected, for both considered CS-microgels at temperatures below the VPT ($\alpha \leq 0.6$), the interactions are purely repulsive when the polymeric shells start to overlap for $R_{IJ} \lesssim 2R_H(\alpha)$.

For standard microgels, it has been demonstrated that in the low-deformability limit, and thus, for low densities, $\Phi^{(2)}$ can be described by a simple Hertzian model [36] for elastic spheres, whose generic pair forces can be written as [37]

$$F_H(R_{IJ}) = \frac{5}{2}\frac{\epsilon_H}{\sigma_H}\left[1 - \frac{R_{IJ}}{\sigma_H}\right]^{3/2} H(1 - R_{IJ}/\sigma_H), \tag{10}$$

where σ_H is the effective elastic diameter, ϵ_H is the strength of the interaction, and $H(x)$ is the Heaviside function. In addition to the clear dependence of the effective elastic diameter on temperature, ϵ_H is also temperature-dependent and further affected by the crosslinker concentration as it is a function of the elastic moduli of the material [36]. To assess the validity of the Hertzian model, we fit the two-body mean forces extracted from the MD simulations using Equation (10) via the ϵ_H parameter and fixing $\sigma_H(\alpha) = 2R_H(\alpha)$. We find that the Hertzian forces match quite well those obtained from the MD simulations at intermediate and long distances, as shown by the dashed lines in Fig. 5(a). This range of forces where the agreement is attained roughly corresponds to $1.5R_H(\alpha) \lesssim R_{IJ} \lesssim 2R_H(\alpha)$, within which the potentials of mean

force satisfy $\Phi_m^{(2)}(R_{IJ}) \lesssim 10\ k_BT$, as exemplified by the CS-microgels at $\alpha = 0.60$ in Fig. 5(b). At shorter distances, the measured forces (and potentials) increase more steeply than predicted by the Hertzian model, similarly to standard microgels [36]. However, we note that the agreement improves when increasing c and therefore the stiffness of the microgels. Hence, despite the layering effects in the polymer distribution, the Hertzian model still describes reasonably well the effective interactions of CS-microgels in the large-separation (high dilution or low-number-density) regime.

At high temperatures ($\alpha = 0.80$), the effective two-body interactions no longer follow the purely elastic Hertzian behavior. Instead, the $\Phi^{(2)}(R_{IJ})$ curves become non-monotonic and develop an attractive well, due to the worsening of the affinity of the monomers to the solvent [38]. Interestingly, the reduced distance at which the effective pair potential reaches its minimum, $R^*_{IJ}/(2R_H(\alpha))$, depends on the crosslinker concentration, shifting to smaller values as c decreases. Since the probed value of α corresponds to the fully collapsed state in experiments—where the polymer's affinity for the solvent is severely reduced—the depth of the effective attraction is quite large, reaching values around $\sim -50k_BT$. Under these conditions, the sampling of the effective forces may be inefficient, but we trust that we have obtained the right qualitative behavior.

3.3.2. Three-body effects

Next, we examine three-body contributions. We note that our goal is not to construct a closed-form, many-body coarse-grained potential for microgels, but to establish unambiguously that their effective interactions are not pairwise additive in the concentrated regime where shells interpenetrate and deform. To this end we focus on a clean diagnostic–three-particle configurations on an equilateral triangle, where triplet effects are generally most pronounced. [39,40] As illustrated in Fig. 6(a), under this symmetric situation, previously considered to study triplet interactions in star polymers [39], the cores of the CS-microgels I, J and K, are located at the corners of an equilateral triangle of side $R_{IJ} = R_{IK} = R_{JK} = R$, while the distance of each particle to the triangle center, C, is $R_{IC} = R_{JC} = R_{KC} = \mathcal{R}$. Due to simple geometrical arguments, under the pairwise approximation, the total effective force on a particle in such configuration is simply $F_m^{(3)\mathrm{p}}(R) = \sqrt{3}F_m^{(2)}(R)$, where the superscript "p" is used to indicate that this corresponds to the total force as evaluated using the effective pair potential. The actual mean force, incorporating three-body contributions, $F_m^{(3)}(R)$, is directly sampled via constrained-bias MD simulations as the average force over the particles in the direction of the circle center:

$$F_m^{(3)}(\mathcal{R}) = \frac{1}{3}\sum_{\ell=1}^{3} \langle \boldsymbol{F}_\ell \cdot \boldsymbol{R}_{\ell C}/R_{\ell C}\rangle_{NVT,\boldsymbol{R}_I,\boldsymbol{R}_J,\boldsymbol{R}_K}. \tag{11}$$

A simple transformation $F_m^{(3)}(\mathcal{R}) \to F_m^{(3)}(R)$ allows for a direct comparison with $F_m^{(3)\mathrm{p}}(R)$. The calculated effective forces on a CS-microgel in the triangle configuration are shown in Fig. 7(a) (dashed lines, 3B), in which we also include the corresponding results for the reference case based on the purely pairwise force (symbols, 2B). The direct comparison allows us to immediately observe that three-body contributions are nonvanishing in both considered CS-microgels, otherwise, $F_m^{(3)}(R)$ would be identical to $F_m^{(3)\mathrm{p}}(R)$, with larger deviations between the two descriptions occurring as the particles become more confined within the triangle. This is due to the greater number of polymer beads from different microgels' shells interacting near the center of the triangle (see Fig. 6(b)).

As in the case of two-body interactions, we find a different behavior below or above the VPT. On one hand, the three-body contributions are attractive when the CS-microgels are in the swollen state below the VPT ($\alpha < 0.60$), where, as discussed above, the two-body potential is purely repulsive at all distances. This implies that neglecting the three-body

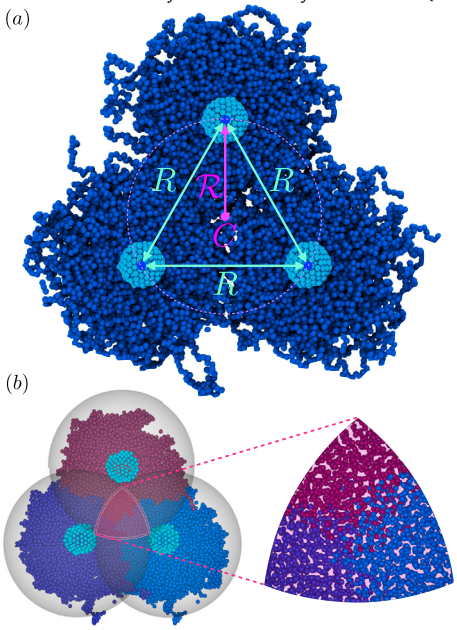

Fig. 6. Three-particle configuration used to determine the effect of three-body interactions of CS-microgels. (a) The cores are placed at the corners of an equilateral triangle of side R, while their distance to the triangle center, C, is $\mathcal{R}$. Note that to aid for a clear appreciation of the core-shell architecture of the microgel, the crosslinked polymeric network is shown only for a hemisphere. (b) At short interparticle distances, three-body effective interactions arise from the simultaneous overlap of the polymeric coronas of three CS-microgels near the center of the triangle formed by their centers. This is schematically illustrated in the simulation configuration: semi-transparent gray spheres—representing the effective particle diameter—highlight the three-body interaction region, with each CS-microgel shown in a different color. In the zoomed-in image, monomer sizes have been reduced for clarity.

contributions in a coarse-grained representation of the CS-microgels below the VPT, as typically done, naturally results in an overestimation of the net repulsive forces experienced by the colloidal particles. This overestimation arises from effectively double-counting overlapping volumes within the pairwise approximation (see Fig. 6(b)). Another plausible explanation for the physical mechanism giving rise to such an attractive three-body contribution is that of a "shared deformation". For instance, when three CS-microgels come close together, two of them (say, I and J) can simultaneously compress the third one (K), sharing the deformation of K in a cooperative way. This shared deformation would then reduce the overall energetic cost compared to the sum of separate pairwise compressions. Attractive effective three-body interactions were also reported by von Ferber et al. [39] for star polymers in a good solvent, where similarly the two-body interactions were purely repulsive. Analogous behavior—repulsive pair interactions accompanied by attractive triplet interactions—has also been observed in systems of charged colloidal spheres under nonlinear conditions, specifically at low salt concentrations and high charges [41].

On the other hand, above the VPT ($\alpha = 0.80$), where CS-microgel two-body potential are attractive, the three-body interactions become repulsive (positive). The denser nature of CS-microgels under these conditions hinders the efficient packing of more than two particles into tight configurations, leading to an excess energy cost in triplets compared to the sum of pairwise interactions. This repulsion can thus be interpreted as arising from "geometric frustration": when a particle approaches a dimer, their mutual attraction is constrained by the excluded volume and rigidity of the collapsed shells, as well as by the increasing steric repulsion from overlapping shells. These factors prevent all three particles from simultaneously optimizing their pairwise contacts. This interpretation is consistent with previous findings

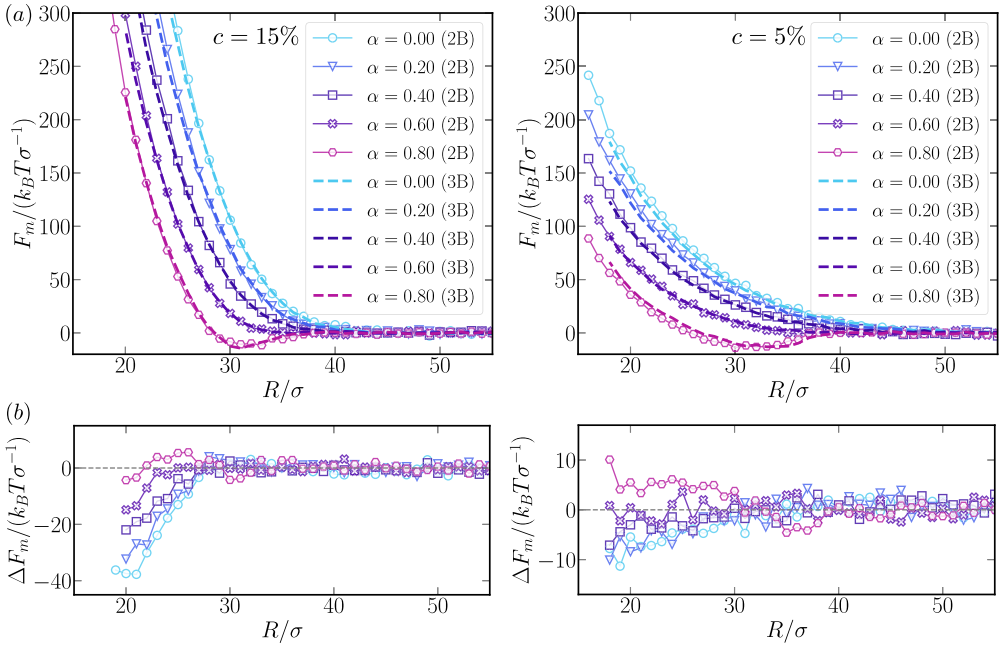

Fig. 7. Effective two- and three-body forces on CS-microgels in a triangular configuration. (a) Mean force on CS-microgels with $c = 5$ and 15% in the three-particle triangular configuration as a function of the mutual distance R (see Fig. 6), under the two-body approximation (2B) and by directly measuring the forces in a three-particle simulation (3B), for various α across the swelling curve. (b) Effective force differences induced by three-body effects.

in other colloidal systems. For example, ligand-stabilized nanoparticles in poor solvent conditions—where dispersion forces dominate the effective attractions—exhibit repulsive three-body contributions due to steric effects [40,21,42]. Similar repulsive three-body terms have also been reported in one-component effective Hamiltonians describing colloid-colloid interactions in the presence of small depletants. In these systems, the three-body repulsion serves to correct for the overestimation of cohesive interactions provided by the two-body Asakura-Oosawa potential [43–46].

To better grasp the deviations between two and three-body contributions and this reversal of trends, Fig. 7(b) shows the difference between the net two-body forces and the measured forces that include three-body contributions, defined as $\Delta F_m(R) = F_m^{(3)}(R) - F_m^{(3)\mathrm{p}}(R)$. Despite statistical uncertainties affecting the mean force measurements, a consistent qualitative trend emerges for both CS-microgels: namely, an increasing discrepancy at small R, and—more importantly—a notable shift in the character of the three-body contribution. Specifically, this contribution transitions from attractive below the VPT ($\Delta F_m < 0$) to predominantly repulsive in the collapsed state ($\Delta F_m > 0$). Interestingly, the difference seems to pass through zero around $\alpha = 0.60$ ($\Delta F_m \approx 0$), where it vanishes over a significant range of mutual separation distances R in which particles are already interpenetrating. We attribute this effect to the balance between the two opposing tendencies above and below the VPT: cooperative deformation, which promotes attraction, and steric frustration, which induces repulsion. One can expect that if these contributions nearly cancel each other close to the VPT temperature, the resulting three-body correction would become negligible, making the effective interactions appear almost pairwise-additive. While the underlying mechanism remains to be fully understood, this seems to be the first observed instance of such a “cancellation” effect.

Overall, we find that whenever the differences between the two approximations are relevant, the relative magnitude of the triplet term, $\Delta F_m/F_m^{(3)\mathrm{p}}$, varies significantly: it ranges between approximately 0.05 and 0.15 for attractive corrections, and between 0.08 and 0.25 for repulsive ones, indicating a relatively small but non-negligible contribution. Interestingly, this range is comparable to that observed in star polymers under good solvent conditions [39].

4. Discussion and conclusions

In this work, we have introduced a novel computational framework for generating thermoresponsive CS-microgels *in silico*, incorporating a solid core and a surface-anchored crosslinker polymer shell. Building on previous works for standard microgels [18,19], we put forward the hypothesis that our model can accurately reproduce key experimental observables of CS-microgels. The present work confirms the ability of our *in silico* microgels to capture swelling curves, density profiles, and scattering form factors across the VPT, providing the robustness of the model and underlining its relevance for the computational study of realistic CS-microgel systems. Our simulations additionally put forward a characteristic signature feature of the structural organization of the polymeric shell in the swollen state, namely a core-induced layering, which, depending on geometrical characteristics, particularly the overall particle to core radius ratio, R_H/R_c, as well as the crosslinker content, may persist or disappear across the swelling curve. The structural rigidity induced by the core-shell interface differentiates these systems from standard microgels and could have important implications for applications at interfaces [14] or in the bottom-up assembly of functional superstructures [47,48].

Using our monomer-resolved model, we have investigated the effective interactions of CS-microgels with relatively thick shells for two different crosslinker concentrations typically employed in experiments. We thus quantified both two- and three-body contributions at varying effective temperature across the VPT. Regardless of the crosslinker concentration, the spherically-symmetric effective pair potentials are repulsive at temperatures below the VPT, turning into attractive at higher temperatures due to the increased solvophobic character. The predominantly elastic response at low temperatures conforms well to Hertzian predictions only at large enough distances, where the degree of interpenetration between the soft colloids is small. However, at smaller separation distances, such a description breaks down as in the case of core-less microgels [36], likely due in part to the heterogeneous inner structure of the polymeric shell and core contributions. Although the CS-microgels studied here possess thick shells and exhibit two-body potentials broadly consistent with those of core-less microgels at modest overlaps, the influence of the core is expected to grow as the shell-

to-core ratio decreases. At small separation distances, the calculated interactions are significantly stiffer than those arising from the Hertzian model, in analogy to standard microgels, for which such increased stiffness has been qualitatively described by a phenomenological extension of the model—the multi-Hertzian model [49]—which assigns varying internal elasticity to particle interactions. Such improved description qualitatively captures experimental behavior at moderate to high volume fractions, but still fails when deformation becomes dominant [50], highlighting the breakdown of two-body approximations and the need for more advanced descriptions that include higher-order interaction terms.

To this aim, we provided the first quantitative investigation of three-body effective interactions in microgels, demonstrating that these contributions are not only non-negligible across the VPT but also undergo a remarkable temperature-dependent sign reversal. At low temperatures (swollen state), three-body effects are attractive, reflecting the flexibility and easy interpenetration of the crosslinked polymeric coronas. In contrast, at high temperatures (collapsed state), they become repulsive as a consequence of the reduced compressibility of the compact shell. While the tunability of two-body interactions—from purely repulsive to attractive—is well established in various types of colloidal systems [51,52], to the best of our knowledge, this is the first reported evidence of such tunability in the character of higher-order effective interaction terms.

Intriguingly, near the VPT, these opposing contributions appear to nearly cancel out over a wide range of interparticle separations, suggesting that the transition marks not only a structural crossover within individual microgels but also a point of minimal many-body influence between them. This can be seen as the manifestation of the VPT in microgels occurring close to the θ-temperature of the underlying polymer, which can be thought as a sort of Boyle temperature from the point of view of effective interactions. This observation may thus justify the use of effective pairwise interactions in theoretical and numerical treatments near the VPT. However, we caution that contributions from higher-order terms beyond three-body cannot be ruled out, especially at high densities. Further investigation is required to fully disentangle the complex and temperature-dependent role of many-body correlations in the collective behavior of thermoresponsive colloids. We envision that the ability to tune many-body effects via microgel architecture and temperature could offer a powerful route for the design of smart materials with specific self-assembling properties.

Overall, our framework provides a flexible and robust platform for probing the rich physics of CS-microgels, both in bulk and at liquid-liquid interfaces, in close connection with experiments. Beyond validating our model against experimental data, our findings also emphasize the need to go beyond pairwise descriptions in coarse-grained models of soft colloids, especially when characterizing deformable systems with complex internal structure. They also offer new insights into how elasticity, morphology, and temperature jointly determine effective interactions in such systems. In the future, machine learning approaches, such as those recently applied to ligand-stabilized nanoparticles [21], could be leveraged to construct computationally efficient coarse-grained models of CS-microgels that systematically incorporate many-body effects. Such developments could open new avenues for studying the collective behavior of CS-microgels, also under confinement or during self-assembly into ordered superstructures via large-scale simulations.

CRediT authorship contribution statement

Gerardo Campos-Villalobos: Writing – review & editing, Writing – original draft, Visualization, Validation, Software, Methodology, Investigation, Formal analysis, Data curation, Conceptualization. **Rodrigo Rivas-Barbosa:** Writing – review & editing, Software, Methodology. **Emanuela Zaccarelli:** Writing – review & editing, Writing – original draft, Supervision, Resources, Project administration, Methodology, Investigation, Funding acquisition, Formal analysis, Conceptualization.

Declaration of competing interest

The authors declare that they have no known competing financial interests or personal relationships that could have appeared to influence the work reported in this paper.

Acknowledgements

G. C.-V. and E. Z. thank Déborah Feller and Matthias Karg for stimulating discussions on various aspects of CS-microgels and for providing the numerical data for CS_1 microgels reported in Fig. 4(c), associated with data in Ref. [15]. We also thank Lorenzo Rovigatti for help in setting up the oxDNA simulations in the presence of the core and Yuri Gerelli for useful discussions on the interpretation of scattering profiles and the comparison between experiments and simulations. G. C.-V. and E. Z. acknowledge funding from European Union HORIZON-MSCA-2024-Postdoctoral Fellowships under agreement no. 101206896, ShapeGels, and from ICSC-Centro Nazionale di Ricerca in High-Performance Computing, Big Data and Quantum Computing-, funded by European Union - NextGenerationEU (Grant No. CN00000013, CUP J93C22000540006, PNRR Investimento M4.C2.1.4). We gratefully acknowledge the CINECA award under the ISCRA initiative, for the availability of high-performance computing resources and support.

Appendix A. Supplementary material

Supplementary material related to this article can be found online at https://doi.org/10.1016/j.jcis.2025.139381.

Data availability

Data supporting this article have been included as part of the Supplementary Material.

References

[1] M. Karg, Functional materials design through hydrogel encapsulation of inorganic nanoparticles: recent developments and challenges, Macromol. Chem. Phys. 217 (2) (2016) 242–255.
[2] T. Hellweg, Responsive core–shell microgels: synthesis, characterization, and possible applications, J. Polym. Sci., Part B, Polym. Phys. 51 (14) (2013) 1073–1083.
[3] J. Oberdisse, T. Hellweg, Recent advances in stimuli-responsive core-shell microgel particles: synthesis, characterisation, and applications, Colloid Polym. Sci. 298 (2020) 921–935.
[4] B. Tadgell, E. Ponomareva, M. Karg, P. Mulvaney, Scattering of visible light by au–pnipam core–shell microgels, J. Phys. Chem. C 126 (36) (2022) 15336–15347.
[5] A.C. Nickel, A.A. Rudov, I.I. Potemkin, J.J. Crassous, W. Richtering, Interfacial assembly of anisotropic core–shell and hollow microgels, Langmuir 38 (14) (2022) 4351–4363.
[6] R. Pelton, Temperature-sensitive aqueous microgels, Adv. Colloid Interface Sci. 85 (1) (2000) 1–33.
[7] A. Rauh, N. Carl, R. Schweins, M. Karg, Role of absorbing nanocrystal cores in soft photonic crystals: a spectroscopy and sans study, Langmuir 34 (3) (2018) 854–867.
[8] Y. Lu, M. Ballauff, Thermosensitive core–shell microgels: from colloidal model systems to nanoreactors, Prog. Polym. Sci. 36 (6) (2011) 767–792.
[9] R. Contreras-Caceres, I. Pastoriza-Santos, R.A. Alvarez-Puebla, J. Perez-Juste, A. Fernandez-Barbero, L.M. Liz-Marzan, et al., Growing au/ag nanoparticles within microgel colloids for improved surface-enhanced Raman scattering detection, Chem. Eur. J 16 (31) (2010) 9462–9467.
[10] M. Mueller, M. Tebbe, D.V. Andreeva, M. Karg, R.A. Alvarez Puebla, N. Pazos Perez, A. Fery, Large-area organization of pnipam-coated nanostars as sers platforms for polycyclic aromatic hydrocarbons sensing in gas phase, Langmuir 28 (24) (2012) 9168–9173.
[11] S. Carregal-Romero, N.J. Buurma, J. Pérez-Juste, L.M. Liz-Marzán, P. Hervés, Catalysis by au@ pnipam nanocomposites: effect of the cross-linking density, Chem. Mater. 22 (10) (2010) 3051–3059.
[12] M. Siebenbürger, M. Fuchs, M. Ballauff, Core–shell microgels as model colloids for rheological studies, Soft Matter 8 (15) (2012) 4014–4024.
[13] K. Geisel, A.A. Rudov, I.I. Potemkin, W. Richtering, Hollow and core–shell microgels at oil–water interfaces: spreading of soft particles reduces the compressibility of the monolayer, Langmuir 31 (48) (2015) 13145–13154.

[14] J. Vialetto, F. Camerin, F. Grillo, S.N. Ramakrishna, L. Rovigatti, E. Zaccarelli, L. Isa, Effect of internal architecture on the assembly of soft particles at fluid interfaces, ACS Nano 15 (8) (2021) 13105–13117.
[15] M. Hildebrandt, D.P. Thuy, J. Kippenberger, T.L. Wigger, J.E. Houston, A. Scotti, M. Karg, Fluid–solid transitions in photonic crystals of soft, thermoresponsive microgels, Soft Matter 19 (37) (2023) 7122–7135.
[16] D. Heyes, A. Brańka, Interactions between microgel particles, Soft Matter 5 (14) (2009) 2681–2685.
[17] S. Maccarrone, A. Ghavami, O. Holderer, C. Scherzinger, P. Lindner, W. Richtering, D. Richter, R.G. Winkler, Dynamic structure factor of core–shell microgels: a neutron scattering and mesoscale hydrodynamic simulation study, Macromolecules 49 (9) (2016) 3608–3618.
[18] N. Gnan, L. Rovigatti, M. Bergman, E. Zaccarelli, In silico synthesis of microgel particles, Macromolecules 50 (21) (2017) 8777–8786.
[19] A. Ninarello, J.J. Crassous, D. Paloli, F. Camerin, N. Gnan, L. Rovigatti, P. Schurtenberger, E. Zaccarelli, Modeling microgels with a controlled structure across the volume phase transition, Macromolecules 52 (20) (2019) 7584–7592.
[20] C.N. Likos, Effective interactions in soft condensed matter physics, Phys. Rep. 348 (4–5) (2001) 267–439.
[21] G. Giunta, G. Campos-Villalobos, M. Dijkstra, Coarse-grained many-body potentials of ligand-stabilized nanoparticles from machine-learned mean forces, ACS Nano 17 (23) (2023) 23391–23404.
[22] F. Sciortino, Three-body potential for simulating bond swaps in molecular dynamics, Eur. Phys. J. E 40 (2017) 1–4.
[23] L. Rank, E. Zaccarelli, Numerical insights on the volume phase transition of thermoresponsive hollow microgels, Soft Matter (2025) 3979–3990, https://doi.org/10.1039/D5SM00057B.
[24] J. Dubbert, T. Honold, J.S. Pedersen, A. Radulescu, M. Drechsler, M. Karg, W. Richtering, How hollow are thermoresponsive hollow nanogels?, Macromolecules 47 (24) (2014) 8700–8708.
[25] P. Šulc, F. Romano, T.E. Ouldridge, L. Rovigatti, J.P. Doye, A.A. Louis, Sequence-dependent thermodynamics of a coarse-grained dna model, J. Chem. Phys. 137 (13) (2012).
[26] G.S. Grest, K. Kremer, Molecular dynamics simulation for polymers in the presence of a heat bath, Phys. Rev. A 33 (5) (1986) 3628.
[27] T. Soddemann, B. Dünweg, K. Kremer, A generic computer model for amphiphilic systems, Eur. Phys. J. E 6 (2001) 409–419.
[28] F.L. Verso, J.A. Pomposo, J. Colmenero, A.J. Moreno, Simulation guided design of globular single-chain nanoparticles by tuning the solvent quality, Soft Matter 11 (7) (2015) 1369–1375.
[29] A. Ninarello, E. Zaccarelli, Hyper-auxeticity and the volume phase transition of polymer gels, Soft Matter (2025).
[30] A.P. Thompson, H.M. Aktulga, R. Berger, D.S. Bolintineanu, W.M. Brown, P.S. Crozier, P.J. In't Veld, A. Kohlmeyer, S.G. Moore, T.D. Nguyen, et al., Lammps-a flexible simulation tool for particle-based materials modeling at the atomic, meso, and continuum scales, Comput. Phys. Commun. 271 (2022) 108171.
[31] J.B. Hubbard, J.F. Douglas, Hydrodynamic friction of arbitrarily shaped Brownian particles, Phys. Rev. E 47 (5) (1993) R2983.
[32] G. Del Monte, D. Truzzolillo, F. Camerin, A. Ninarello, E. Chauveau, L. Tavagnacco, N. Gnan, L. Rovigatti, S. Sennato, E. Zaccarelli, Two-step deswelling in the volume phase transition of thermoresponsive microgels, Proc. Natl. Acad. Sci. USA 118 (37) (2021) e2109560118.
[33] N. Hazra, A. Ninarello, A. Scotti, J.E. Houston, P. Mota-Santiago, E. Zaccarelli, J.J. Crassous, Structure of responsive microgels down to ultralow cross-linkings, Macromolecules 57 (1) (2023) 339–355.
[34] P.N. Pusey, Introduction to scattering experiments, in: T.Z.P. Lindner (Ed.), Neutron, X-Rays and Light. Scattering Methods Applied to Soft Condensed Matter, Elsevier Science B. V., 2002, pp. 3–22.
[35] G. Ciccotti, M. Ferrario, J.T. Hynes, R. Kapral, Constrained molecular dynamics and the mean potential for an ion pair in a polar solvent, Chem. Phys. 129 (2) (1989) 241–251.
[36] L. Rovigatti, N. Gnan, A. Ninarello, E. Zaccarelli, Connecting elasticity and effective interactions of neutral microgels: the validity of the hertzian model, Macromolecules 52 (13) (2019) 4895–4906.
[37] L.D. Landau, L. Pitaevskii, A.M. Kosevich, E.M. Lifshitz, Theory of Elasticity, vol. 7, vol. 7, Elsevier, 2012.
[38] S. Chen, X. Yong, Elastocapillary interactions of thermoresponsive microgels across the volume phase transition temperatures, J. Colloid Interface Sci. 584 (2021) 275–280.
[39] C. Von Ferber, A. Jusufi, C. Likos, H. Löwen, M. Watzlawek, Triplet interactions in star polymer solutions, Eur. Phys. J. E 2 (2000) 311–318.
[40] P. Schapotschnikow, T.J. Vlugt, Understanding interactions between capped nanocrystals: three-body and chain packing effects, J. Chem. Phys. 131 (12) (2009).
[41] C. Russ, H. Von Grünberg, M. Dijkstra, R. van Roij, Three-body forces between charged colloidal particles, Phys. Rev. E 66 (1) (2002) 011402.
[42] G. Bauer, N. Gribova, A. Lange, C. Holm, J. Gross, Three-body effects in triplets of capped gold nanocrystals, Mol. Phys. 115 (9–12) (2017) 1031–1040.
[43] M. Dijkstra, J.M. Brader, R. Evans, Phase behaviour and structure of model colloid-polymer mixtures, J. Phys. Condens. Matter 11 (50) (1999) 10079.
[44] M. Dijkstra, R. van Roij, R. Roth, A. Fortini, Effect of many-body interactions on the bulk and interfacial phase behavior of a model colloid-polymer mixture, Phys. Rev. E, Stat. Nonlinear Soft Matter Phys. 73 (4) (2006) 041404.
[45] G. Campos-Villalobos, E. Boattini, L. Filion, M. Dijkstra, Machine learning many-body potentials for colloidal systems, J. Chem. Phys. 155 (17) (2021).
[46] G. Campos-Villalobos, G. Giunta, S. Marín-Aguilar, M. Dijkstra, Machine-learning effective many-body potentials for anisotropic particles using orientation-dependent symmetry functions, J. Chem. Phys. 157 (2) (2022).
[47] M.A. Boles, M. Engel, D.V. Talapin, Self-assembly of colloidal nanocrystals: from intricate structures to functional materials, Chem. Rev. 116 (18) (2016) 11220–11289.
[48] D. Suzuki, J.G. McGrath, H. Kawaguchi, L.A. Lyon, Colloidal crystals of thermosensitive, core/shell hybrid microgels, J. Phys. Chem. C 111 (15) (2007) 5667–5672.
[49] M.J. Bergman, N. Gnan, M. Obiols-Rabasa, J.-M. Meijer, L. Rovigatti, E. Zaccarelli, P. Schurtenberger, A new look at effective interactions between microgel particles, Nat. Commun. 9 (1) (2018) 5039.
[50] G. Del Monte, E. Zaccarelli, Numerical study of neutral and charged microgel suspensions: from single-particle to collective behavior, Phys. Rev. X 14 (4) (2024) 041067.
[51] A. Yethiraj, Tunable colloids: control of colloidal phase transitions with tunable interactions, Soft Matter 3 (9) (2007) 1099–1115.
[52] R. Evans, D. Frenkel, M. Dijkstra, From simple liquids to colloids and soft matter, Phys. Today 72 (2) (2019) 38–39.